

Casimir Effect on the Worldline

Holger Gies^{b,c}, Kurt Langfeld^a, Laurent Moyaerts^a^a Institut für Theoretische Physik, Universität Tübingen
D-72076 Tübingen, Germany^b CERN, Theory Division, CH-1211 Geneva 23, Switzerland^c Institut für theoretische Physik, Universität Heidelberg
D-69120 Heidelberg, Germany

March 2003

Abstract

We develop a method to compute the Casimir effect for arbitrary geometries. The method is based on the string-inspired worldline approach to quantum field theory and its numerical realization with Monte-Carlo techniques. Concentrating on Casimir forces between rigid bodies induced by a fluctuating scalar field, we test our method with the parallel-plate configuration. For the experimentally relevant sphere-plate configuration, we study curvature effects quantitatively and perform a comparison with the "proximity force approximation", which is the standard approximation technique. Sizable curvature effects are found for a distance-to-curvature-radius ratio of $a/R \lesssim 0.02$. Our method is embedded in renormalizable quantum field theory with a controlled treatment of the UV divergencies. As a technical by-product, we develop various efficient algorithms for generating closed-loop ensembles with Gaussian distribution.

1 Introduction

The Casimir effect [1] has recently been under intense study, experimentally [2] as well as theoretically (for recent comprehensive reviews, see [3]). In fact, we are currently witnessing a transition of the Casimir effect from a pure fundamental quantum effect, being interesting in its own right, via an experimentally challenging problem to a phenomenon becoming relevant to applied physics such as nanotechnology [4]. Moreover, the Casimir effect has been suggested as an experimentally powerful tool for investigating new physics beyond the standard model [5].

Considerable progress has been made in recent years as far as the Casimir effect of real (rather than idealized) conductors is concerned: the effects of finite conductivity, finite temperature, and surface roughness are theoretically well under control for the current experimental realizations. Even the dependence of the Casimir force on the isotopic composition of the interacting bodies has been studied recently [6]. By contrast, the dependence of the Casimir force on the geometry of the interacting bodies is neither completely understood nor quantitatively satisfactorily under control. Except for a small number of analytically solvable geometries, one has to rely on approximations among which the "proximity force approximation" [7, 8] represents the most widely used method. Roughly speaking, the proximity force approximation maps the Casimir effect of an arbitrary geometry onto Casimir's parallel-plate configuration, thereby neglecting curvature and tilt effects in an uncontrolled manner. In fact, the current limitations for a quantitative comparison of theory and experiment arise essentially from an estimated 1% error of the proximity force approximation.

The basic obstacles against improving this situation are mainly technical in nature and partly fundamental. Standard strategies perform the Casimir calculations in two steps: first, the mode spectrum of quantum fluctuations in a given background geometry has to be identified; secondly, the Casimir energy is obtained by summing up (tracing over) the spectrum. The first step is obviously increasingly difficult the more complex a given geometry is; without a high degree of symmetry, even the use of standard numerical techniques is rather limited. The second step suffers from the same problems, but is moreover complicated by the fact that the mode sum is generally ultraviolet divergent. The divergencies have to be analyzed and, if possible, be removed by renormalization of physical parameters. Not only is the handling of these divergencies technically (and numerically) challenging, but the classification of divergencies is also still under intense debate [9, 10, 11].

In this work, we propose a method that has the potential to solve these technical problems. Moreover, it is embedded in perturbative quantum field theory with its clear and unambiguous renormalization program. Our method is based on the "string-inspired" worldline formalism in which perturbative N -point amplitudes are mapped onto quantum mechanical path integrals over closed worldlines [12] (for a recent review, see [13]). The technical advantages arise from the fact that the mode spectrum and its sum are not computed separately but all at once. These worldline integrals can conveniently be calculated with Monte-Carlo methods (worldline numerics) with an algorithm that is completely in-

dependent of the Casimir geometry; in particular, no background symmetry is required. Whereas the worldline integral is finite, the ultraviolet divergencies occur in a "proper time" integral, roughly corresponding to an integral over the size of the worldlines. The divergencies can be found at small proper times (\Leftrightarrow small size \Leftrightarrow ultraviolet), where a mapping to Feynman-diagram language is possible and the standard rules of renormalization can be applied.

In order to illustrate our method, we focus in this work on the calculation of Casimir forces between rigid bodies, induced by quantum fluctuations of a scalar field. The rigid bodies are modeled by background potentials $V(x)$ (mainly of δ -function type), which allow us to approach the idealized limit of Dirichlet boundary conditions in a controlled way. As a benchmark test, we study the classic parallel-plate configuration in detail. Finally, we compute the Casimir forces between a plate and a cylinder as well as the experimentally highly relevant case of a plate and a sphere, both in the idealized Dirichlet limit. Here we find clear signals of curvature effects if the distance between the bodies is roughly a few percent of the cylinder/sphere radius or larger. This scale characterizes the limit of quantitative accuracy of the proximity force approximation.

We developed the technique of worldline numerics in [14] and it has successfully been applied to the computation of quantum energies or actions induced by scalar or fermion fluctuations in electromagnetic backgrounds [14, 15, 16]. As for any numerical method, possible finite-size or discretization errors have to be analyzed carefully. In this respect, the idealized Casimir problem turns out to be most challenging, because the background potentials with their δ -like support affect the quantum fields on all scales. Therefore, we have to make sure that our worldline numerics operates sufficiently close to the "continuum limit" (proper time continuum in our case). We dedicate a whole section (Sect. 3) to this question, also relevant for further applications of worldline numerics, and present a number of new and efficient algorithms for the generation of Gaussian distributed closed-loop ensembles.

Though the heart of our method is intrinsically numerical, we would like to emphasize that the worldline technique offers an intuitive approach to quantum phenomena. Particularly for Casimir forces between rigid bodies, many features such as the sign of the interaction or curvature effects can easily be understood when thinking in terms of worldline ensembles (loop clouds).

The paper is organized as follows: the next section provides a brief introduction into the worldline approach to the Casimir effect. Section 3 describes efficient methods for the generation of loop ensembles. The reader who is mainly interested in Casimir phenomenology may skip this section. Section 4 provides for an intuitive understanding of rigid-body Casimir forces in the light of the worldline language. Our numerical findings for the rigid-body Casimir force for several geometries (plate-plate, plate-sphere, plate-cylinder) are presented in section 5.

2 Worldline techniques for Casimir configurations

2.1 Framework

Let us discuss the formalism for the simplest case of a real scalar field coupled to a background potential $V(\mathbf{x})$ by which we describe the Casimir configuration. The field theoretic Lagrangian is

$$L = \frac{1}{2} \partial_\mu \phi \partial^\mu \phi + \frac{1}{2} m^2 \phi^2 + \frac{1}{2} V(\mathbf{x}) \phi^2; \quad (1)$$

The potential $V(\mathbf{x})$ can be considered as a spacetime dependent mass squared, implying that it has mass dimension 2. In the absence of any further fields and couplings, the complete unrenormalized quantum effective action for V is

$$\begin{aligned} [V] &= \frac{1}{2} \text{Tr} \ln \frac{\partial^2 + m^2 + V(\mathbf{x})}{\partial^2 + m^2} \\ &= \frac{1}{2} \int_{T=1}^{T=Z} \frac{dT}{T} \int d^D \mathbf{x} \int_{\mathbf{j}^T} \langle \mathbf{x} | \mathcal{P}^{T(\partial^2 + m^2 + V(\mathbf{x}))} | \mathbf{j} \rangle \frac{1}{(4\pi T)^{D/2}} e^{m^2 T}; \quad (2) \end{aligned}$$

Here we work in $D = d + 1$ Euclidean spacetime dimensions, i.e., d space dimensions. In the second line of Eq. (2), we have introduced the proper time representation of the $\text{Tr} \ln$ with an UV cutoff at the lower bound of the T integral.¹ Interpreting the matrix element as a quantum mechanical transition amplitude in proper time T , we can introduce the path integral, or worldline, representation,

$$[V] = \frac{1}{2} \frac{1}{(4\pi)^{D/2}} \int_{T=1}^{T=Z} \frac{dT}{T^{1+D/2}} e^{m^2 T} \int d^D \mathbf{x} \int_{\mathbf{y}}^{\mathbf{E}} W_V[\mathbf{y}(t)] \mathbf{1}; \quad (3)$$

where we introduced the "Wilson loop"

$$W_V[\mathbf{y}(t)] = \exp \left[-T \int_0^Z dt V(\mathbf{x} + \frac{\mathbf{p}}{T} \mathbf{y}(t)); \quad (4) \right.$$

and

$$W_V[\mathbf{y}]_{\mathbf{y}}^{\mathbf{E}} = \frac{\int_{\mathbf{y}(0)=\mathbf{y}(1)}^{\mathbf{R}} D\mathbf{y} W_V[\mathbf{y}] e^{\int_0^R dt \mathbf{y}^2 = 4}}{\int_{\mathbf{y}(0)=\mathbf{y}(1)}^{\mathbf{R}} D\mathbf{y} e^{\int_0^R dt \mathbf{y}^2 = 4}} \quad (5)$$

denotes the expectation value of an operator with respect to a path integral over unit loops $\mathbf{y}(t)$, which are closed worldlines parametrized by a unit proper time $t \in [0; 1]$; all unit loops have a common center of mass which is set to zero, $\int_0^1 dt \mathbf{y}(t) = 0$. This construction of

¹Other regularization techniques are possible as well, e.g., dimensional regularization, $(dT=T^{-1})$!
² $(dT=T^{-1})$; the proper time cutoff is used only for the sake of definiteness. For a pedagogical review of various regularization techniques in the Casimir context, see [17].

Eq. (3) is exact and completely analogous to the one proposed in [14] for electromagnetic backgrounds; further details can be found therein.

For time-independent Casimir configurations, we can carry out the time integration trivially, $\int dx_0 = L_{x_0}$, where L_{x_0} denotes the "volume" in time direction, and define the (unrenormalized) Casimir energy as

$$E = -L_{x_0} : \quad (6)$$

2.2 Renormalization

The analysis of divergencies in Casimir calculations is by no means trivial, as the ongoing debate in the literature demonstrates [10, 11]. The reason is that divergencies in these problems can have different sources with different physical meaning. On the one hand, there are the standard field theoretic UV divergencies that can be mapped onto divergencies in a finite number of Feynman diagrams at a given loop order; only these divergencies can be removed by field theoretic renormalization, which is the subject of the present section.

On the other hand, divergencies can arise from the physical modeling of the Casimir boundary conditions. In particular, idealized conditions such as perfectly conducting surfaces affect quantum fluctuations of arbitrarily high frequency; therefore, an infinite amount of energy may be required to constrain a fluctuating field on all scales. These divergencies are real and imply that idealized conditions can be ill-defined in a strict sense. The physically important question is whether these divergencies affect the physical observable under consideration (such as Casimir forces) or not. If not, the idealized boundary conditions represent a simplifying and valid assumption, and the removal of these divergencies can be justified. But if the observable is affected, the idealized conditions have to be dropped, signaling the strong dependence of the result on the physical details of the boundary conditions (e.g., material properties).

Even though the worldline is an appropriate tool for analyzing both types of divergencies, we concentrate on the first type in this paper, leaving a discussion of the second for future work.

In order to isolate the field theoretic UV divergencies, we can expand the proper-time integrand for small proper-times (high momentum scales). Since this is equivalent to a local gradient expansion in terms of the potential $V(x)$ (heat-kernel expansion), each term $\int V(x)^n$ corresponds to a scalar one-loop Feynman diagram with n external legs coupling to the potential $V(x)$ and its derivatives, and with the momentum integration already performed (thanks to the worldline method). Using $\int_0^1 dt y(t) = 0$ and $\int_0^1 dt y(t) y(t) i_y = (1=6)$, we find up to order T^2 ,

$$\int_x \hbar W_V = \int_x \frac{1}{4} = \int_x T \int^{Z} d^D x V(x) + \frac{T^2}{6} \int_x d^D x \partial^2 V(x) + \frac{T^2}{2} \int_x d^D x V(x)^2 + O(T^3); \quad (7)$$

which should be read together with the propagator factor $1/T^{1+D=2}$ in Eq. (3). The term $V(x)$ corresponds to the tadpole graph. In the conventional "no-tadpole" renormalization scheme, the renormalization counterterm $V(x)$ is chosen such that it cancels the tadpole contribution completely. Of course, any other renormalization scheme can be used as well. The corresponding counterterm can be fixed unambiguously by an analysis of the tadpole Feynman diagram in the regularization at hand. In $D < 4$ spacetime dimensions, there is no further counterterm, since $V(x)$ has mass dimension 2. The remaining terms of $O(T^2)$ are UV finite in the limit $T \rightarrow 0$.

In $4 < D < 6$, we need further subtractions. Here, it is useful to note that the last term on the first line of Eq. (7) vanishes anyway, provided that the potential is localized or drops off sufficiently fast at infinity. This is, of course, always the case for physical Casimir configurations.² Renormalization provides us with a further counterterm $\int_x V^2$ subject to a physically chosen renormalization condition such that the divergence arising from the last T^2 term is canceled. With this renormalization condition, the physical value of the renormalized operator $\int_x V^2$ is fixed.³ For even higher dimensions, similar subtractions are required that involve higher-order terms not displayed in Eq. (7).

As far as controlling divergencies by renormalization is concerned, this is all there is and no further ad hoc subtractions are permitted. However, having removed these UV divergencies with the appropriate counterterms does not guarantee that the resulting Casimir energy is finite. Further divergencies may arise from the form of the potential as is the case for the idealized Casimir energies mentioned above.

In the present work, we take up a more practical position and are merely interested in the Casimir forces between disconnected rigid bodies which are represented by the potential $V(x) = V_1(x) + V_2(x) + \dots$. We assume the rigid bodies as given, disregarding the problem of whether the Casimir energy of every single body is well defined by itself. For this, it suffices to study the interaction Casimir energy defined as the Casimir energy of the whole system minus the separate energies of the single components,

$$E := E_{V=V_1+V_2+\dots} - E_{V_1} - E_{V_2} - \dots \quad (8)$$

Note that the subtractions do not contribute to the Casimir force which is obtained by differentiating the interaction energy with respect to parameters that characterize the separation and orientation of the bodies. By this differentiation, the subtractions drop out. Furthermore, these terms remove the old theoretic UV divergencies of Eq. (7): this is obvious for the terms linear in $V(x)$; for the quadratic one, this follows from $\int_x V^2 = \int_x (V_1 + V_2 + \dots)^2 = \int_x (V_1^2 + V_2^2 + \dots)$. The last equation holds because of the local support

²Strictly speaking, infinitely extended surfaces such as idealized infinitely large plates do not belong to this class, but we can always think of large but finite surfaces and then take the infinite-surface limit after the infinite-volume limit.

³Since we used a gradient expansion, the renormalized operator is fixed in the small-momentum limit; if the renormalization condition operates at finite momentum, e.g., using the polarization operator, possible finite renormalization shifts can be obtained from an analysis of the corresponding Feynman diagram. However, in the present case of static Casimir problems, it is natural to impose a renormalization condition in the small-momentum limit anyway.

of the disconnected bodies. By the same argument, the subtractions remove every term of a local expansion of $E_{V_1+V_2+\dots}$ to any finite order. In this way, any divergence induced locally by the potentials is canceled. But, of course, the Casimir force is not removed (it is inherently nonlocal).

We would like to stress that the definition of the interaction energy in Eq. (8) should not be confused with renormalization. It is a procedure for extracting exact information about the Casimir force between rigid bodies, circumventing the tedious question as to whether Casimir energy densities are locally well defined. This procedure also removes the old theoretic UV divergencies. In this case, renormalization conditions which fix the counter terms do not have to be specified. These local counter terms cannot exert an influence on the Casimir force for disconnected rigid bodies anyway, because the latter is a nonlocal phenomenon. Expressed in physical terms of the QED Casimir effect: the renormalized strength of the coupling between the electromagnetic field and the electrons in the metal is, of course, important for a computation of the local energy density near a plate, but the Casimir force between two plates is independent of the electromagnetic coupling constant.

We would like to point out that the concept of the interaction energy is meaningless for the computation of Casimir stresses of single bodies, e.g., a sphere. Here, the renormalization procedure has to be carried out as described above, and the result may depend on the renormalization conditions and strongly on the details of the potential.

3 Worldline numerics

In this section, we discuss possible numerical realizations of the worldline integral Eqs. (3)–(5) (the more phenomenologically interested reader may proceed directly to Sect. 4).

As proposed in [14], we estimate the analytical integral over infinitely many closed worldlines by an ensemble average over infinitely many closed loops obeying a Gaussian velocity distribution $P[\dot{y}(t)g]$,

$$P[\dot{y}(t)g] = \int_0^1 dt y(t) \exp\left[-\frac{1}{4} \int_0^1 dt \dot{y}^2\right]; \quad \text{with } y(0) = y(1); \quad (9)$$

where the constraint ensures that the loops are centered upon a common center of mass (here and in the following, we drop all normalizations of the distributions, because they are irrelevant when taking expectation values). Here, we have chosen to work with rescaled unit loops $y(t)$ as introduced in Eqs. (3)–(5). Numerical arithmetic requires discretization; however, we generally do not discretize spacetime on a lattice, but only the loop parameter t :

$$\dot{y}(t)g \quad \rightarrow \quad \dot{y}_k g \in \mathbb{R}^D; \quad k = 1; 2; \dots; N; \quad (10)$$

where N denotes the number of points per loop (ppl). Whereas Gaussian distributed numbers can easily be generated, the numerical difficulty is to impose the constraint, $y_1 + y_2 + \dots + y_N = y(0)$, and the requirement of closeness. In the following, we discuss four possible algorithms, and recommend the last two of them based on Fourier decomposition ("fbops") or explicit diagonalization ("vbops").

3.1 Heat-bath algorithm

A standard approach for the generation of field (or path) distributions that obey a certain action is the heat-bath algorithm, which has been employed for worldline numerics in [14, 15, 16]. Discretizing the derivative in the exponent of Eq. (9), e.g., by $\underline{y} = \{y_k\}_{k=1}^N$, each point on a loop can be regarded as exposed to a "heat bath" of all neighboring points. The discretized probability distribution then reads

$$P(\underline{y}_k) = \int_{y_1}^{y_2} \dots \int_{y_N}^{y_{N+1}} \exp\left[-\frac{N}{4} \sum_{k=1}^N (y_k - y_{k-1})^2\right] \mathcal{D}\underline{y} \quad (11)$$

where $y_0 = y_N$. The heat-bath procedure now consists in the following steps: (i) choose a site $i \in \{1, \dots, N\}$, consider all variables y_k , $k \neq i$ as constant, and generate the y_i according to its probability; (ii) visit all variables of the loops (e.g., in a serial fashion or using the checkerboard algorithm). Thereby, the closeness requirement is easily realized with, e.g., y_N being in the heat bath of y_{N-1} and y_1 , etc. The center-of-mass constraint can be accommodated by shifting the whole loop correspondingly after one thermalization sweep (update of all points per loop).

Whereas this procedure has been sufficient for the applications discussed in [14, 15, 16], it turns out that this algorithm suffers in practice from a thermalization problem for large values N . To demonstrate this, let us define the extension e of the loop ensemble by the loop mean square

$$e^2 = \frac{1}{N} \int \mathcal{D}\underline{y} \sum_{k=1}^N y_k^2 P(\underline{y}_k); \quad N = \int \mathcal{D}\underline{y} P(\underline{y}_k) \quad (12)$$

This quantity can be calculated analytically, straightforwardly yielding

$$e = \frac{1}{6} \left(1 + \frac{1}{N^2}\right) \quad (13)$$

In order to generate a "thermalized" loop, one starts with a random ensemble \underline{y}_k and performs $s n_t$ heat-bath sweeps. For each loop, we calculate its extension e . After averaging over 1000 loops, we compare the estimator of e as function of n_t with the analytic result (13) corresponding to the limit $n_t \rightarrow \infty$.

The result is shown in Fig. 1. One clearly observes that the thermalization of loop ensembles is expensive for $N > 500$. In fact, roughly $n_t = 45000$ is needed for an acceptable loop ensemble consisting of $N = 1000$ points. Since a computation of Casimir energies requires loop ensembles of $N \approx 1000$, the heat-bath algorithm is too inefficient and cannot be recommended.

3.2 Random Walk

In order to circumvent the thermalization problem, one may exploit the connection between loops with Gaussian velocity distribution and random walks [18, 19]. This has been adapted

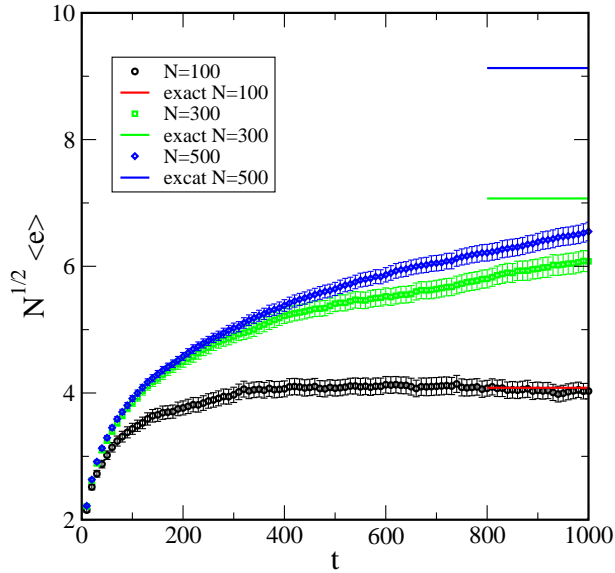


Figure 1: The average extension $\langle e \rangle$ (multiplied by $N^{1/2}$ for better visualization) of the loops as function of the number of thermalizations t .

to worldline numerics with latticized spacetime in [20]; here, however, we keep spacetime continuous. For this purpose, let us give up the concept of unit loops for a moment, and reinstate the naturally emerging coordinate space loops $x(\cdot)$,

$$x(\cdot) = \frac{1}{T} y(\cdot = T); \quad x(0) = x(T): \quad (14)$$

Probability theory tells us that random walks automatically implement the Gaussian velocity distribution

$$N^{1/2} \exp \left[-\frac{1}{4} (x_{i+1} - x_i)^2 \right] : \quad (15)$$

The crucial point is to establish the relation between a loop that a random walker with step length a would generate for us and a thermalized loop at a given proper time T . This relation results from a coarse-graining procedure, which we present here briefly. Given that the random walker starts at the point x_i , the probability density for reaching the point x_f after n steps is given by

$$p(x_f | x_i; n; a) = \int d^D x_2 \dots d^D x_{n-1} \prod_{k=1}^{n-1} \frac{1}{(D) a^{D-1}} (x_{k+1} - x_k | a);$$

with (D) being the solid angle in D dimensions, $x_1 = x_i$ and $x_n = x_f$. For $n \gg 1$, but na^2 fixed, the central-limit theorem can be applied [19]:

$$\lim_{n \rightarrow \infty} p(x_f | x_i; n; a) = \frac{D}{2} \frac{1}{na^2} \exp \left[-\frac{D}{2na^2} (x_f - x_i)^2 \right]; \quad na^2 = \text{fixed}: \quad (16)$$

Comparing (16) with (15), one identifies

$$= \frac{na^2}{2D}; \quad (17)$$

The dimension of the property as well as its relation to the loop length L appears here in an obvious way,

$$T = \frac{N_w a^2}{2D} = \frac{La}{2D}; \quad (18)$$

where N_w now is the total number of walker steps. It is important to point out that the property can be tuned in two ways: we can adjust either the walker step a or the number of points N_w . The corresponding two methods to generate a loop ensemble at given property T work as follows:

Method 1: a is fixed.

- (1) choose the walker step a ;
- (2) read off from Eq. (18) the number of points N_w corresponding to T ;
- (3a) generate N_w points by letting a random walker go N_w steps, and accept the configuration if the last step leads him into a small sphere (radius ϵ) centered upon the starting point;
- (3b) close the loop 'by hand' by shifting the last point to the starting point;
- (4) shift the center of mass to zero;
- (5) repeat steps (3) and (4) n_L times for an ensemble of n_L loops.

We point out that the value of a must be much smaller than the characteristic length scale provided by the background potential. A second constraint on a arises from the applicability of the central limit theorem, i.e., $n \gg 1$ in (16). A third systematic numerical uncertainty follows from the shift in step (3b). Unfortunately, small values for ϵ result in low acceptance rate for loops, and, therefore, increase the numerical effort to generate the loop ensemble. A good compromise is to set the radius ϵ to some percentage of the step length a .

For illustration only, we leave the Casimir effect for a second and consider the average Wilson Loop $\langle W_V \rangle$ (see Eq. (5)) for the case of a constant magnetic background field $\vec{B} = B \hat{e}_z$ at $T = 1$ and $D = 2$,

$$V(\mathbf{x}) = A_k(\mathbf{x}) x_k; \quad \vec{A} = B = 2(y; x; 0);$$

For $T = 1$ the walker step length is given by $a = \sqrt{\frac{2}{N_w}}$. Figure 2 shows our numerical result as a function of N_w in comparison with the exact value. Circles with error bars correspond to loop ensembles generated with $\epsilon = 0.05 a$. The limit (16) seems to be attained for $50 < N_w < 100$ ($a < 0.3$). For a further improvement of the numerical accuracy, large values of N_w and a decrease of ϵ at the same time are required. Finally, we point out that

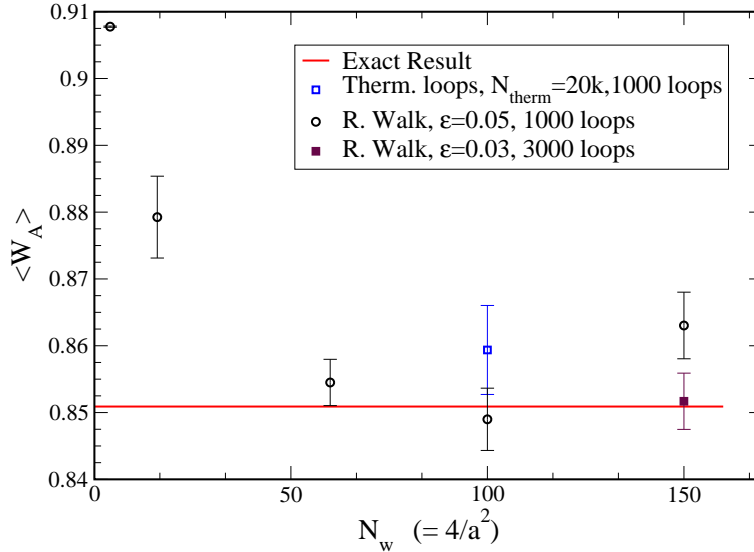


Figure 2: Average Wilson Loop $\langle W_A \rangle$ (cf. Eq. (5)) for the case of a constant magnetic background field B for $B = 1, T = 1$ and $D = 2$ as a function of the number of points per loop.

the deviation from the exact result in the case of the heat-bath-generated loop ensemble (blue square) is probably due to thermalization effects.

Note that we have to generate a loop ensemble for each value of T ($N_w a^2$), which makes this procedure far more memory consuming than the heat-bath approach. If we decide to generate the loop ensembles once and for all and save them to disk, we have to handle huge amounts of data. On the other hand, if we create our loops 'on demand' (while performing the T or κ integrations), we are confronted with a serious waste of computing time.

Method 2: N_w is fixed.

- (1) choose the number of points N_w ;
- (2) set the walker step to $a = 1$;
- (3) proceed with steps (3), (4) and (5) of the first method.

The loop ensemble is here generated only once and then rescaled to adjust the step length to the value a corresponding to T in (18). This method therefore works as in the case of the rescalable thermalized unit loops, with the difference that the proportionate rescaling is realized via the rescaling of the step length. This tuning at the level of a provides for a better control of the microscopic features of the loops. The second procedure is thus a good candidate to replace the thermalized loops since it combines the absence of thermalization and the rescaling of an all-at-once generated ensemble.

It should however be emphasized that most of the computer time is spent on generating redundant open loops. This is due to the fact that, for a given N_w , the fraction of loops which close after N_w steps decreases like $N_w^{-D/2}$.

3.3 Fourier decomposition: "f loops"

We are now looking for alternative methods that could combine some advantages of the two previous approaches and bypass the problems rendering them impractical. A highly efficient procedure arises from a Fourier representation of our unit loops

$$y(t) = \sum_{i=0}^{N-1} a_i \cos 2\pi t + b_i \sin 2\pi t; \quad a_0 = 0; \quad (19)$$

where N is the number of Fourier modes included (which agrees with the number of points specifying each loop, see below). The choice $a_0 = 0$ guarantees that the loop center of mass is located at the origin. Inserting Eq. (19) into Eq. (9), the probability distribution for the coefficients is given by

$$P(a_i; b_i) = \exp \left[-\frac{1}{2} \sum_{i=1}^{N-1} a_i^2 - \frac{1}{2} \sum_{i=0}^{N-1} b_i^2 \right]; \quad (20)$$

We can then take advantage of the fact that the Fourier components $f_i; b_i$ are not correlated, in order to generate our loops in momentum space. The reconstruction of the unit loop $y(t)$ in Eq. (19) is most efficiently performed by using the fast Fourier transform (FFT). For these purposes, we define complex coefficients $c_i = a_i + ib_i$, and obtain

$$y(t) = \sum_{i=0}^{N-1} c_i \exp(i 2\pi t); \quad (21)$$

The FFT procedure generates a series of points $y_i, i = 0 ::: N-1$ which discretize the continuous curve $y(t)$ and thereby constitute the unit loops.

3.4 Explicit diagonalization: "v loops"

Finally, we propose an algorithm that is based on a linear variable transformation $f_{k,g} \rightarrow v_{k,g}$, such that the discretized distribution (11) becomes purely Gaussian. These new variables are velocity-like and diagonalize the quadratic form in the exponent.

Because of the δ function in Eq. (11), only $N-1$ coordinates per loop are independent. Defining $\int_{-R_1}^{R_1} \prod_{i=1}^{N-1} dy_i$, we may perform, e.g., the y_N integration using the δ function,

$$\begin{aligned} \int_{-R_1}^{R_1} \prod_{i=1}^{N-1} dy_i P_{f_{k,g}} &::: = \int_{-R_1}^{R_1} \prod_{i=1}^{N-1} dy_i e^{[\frac{N}{4} \left(\sum_{i=2}^{N-1} (y_i - y_{i-1})^2 + (2y_1 + y_2 + \dots + y_{N-1})^2 + (y_1 + y_2 + \dots + 2y_{N-1})^2 \right)]} ::: \\ &=: \int_{-R_1}^{R_1} \prod_{i=1}^{N-1} dy_i e^{[\frac{N}{4} Y]} :::; \end{aligned} \quad (22)$$

where the dots represent an arbitrary y -dependent operator, and we introduced the abbreviation Y for the quadratic form. In order to turn the exponential into a product of simple Gaussians, we define $N-1$ new velocity-like variables,

$$\begin{aligned} v_1 &:= \frac{3}{2}Y_1 + Y_2 + Y_3 + \dots + Y_{N-1}; \\ v_i &:= Y_i - Y_1; \quad i=2;3;\dots;N-1; \end{aligned} \quad (23)$$

For notational simplicity, it is useful to also introduce the auxiliary variable,

$$v_{i;j} = v_i + v_{i1} + \dots + v_{j1} - Y_j; \quad \text{for } i, j = 1;2;\dots;N-1; \quad (24)$$

such that the exponent Y can be written as

$$\begin{aligned} Y &= \sum_{i=2}^{N-1} v_i^2 + v_1 \left[\frac{1}{2}v_{N-1;1}^2 + v_1 + \frac{1}{2}v_{N-1;1}^2 \right] \\ &= 2v_1^2 + \frac{1}{2}v_{N-1;1}^2 + \sum_{i=2}^{N-1} v_i^2; \end{aligned} \quad (25)$$

We observe that the variable v_1 now appears quadratically in the exponent as desired. The same has still to be achieved for $v_2 \dots v_{N-1}$. For this, we note that $v_{N-1;1} = v_{N-1} + v_{N-2;1}$ by definition (24). Defining

$$v_{N-1} := v_{N-1} + \frac{1}{3}v_{N-2;1}; \quad (26)$$

we indeed obtain for the exponent Y

$$\begin{aligned} Y &= 2v_1^2 + v_{N-1}^2 + \frac{1}{2}(v_{N-1} + v_{N-2;1})^2 + \sum_{i=2}^{N-2} v_i^2 \\ &= 2v_1^2 + \frac{3}{2}v_{N-1}^2 + \frac{1}{3}v_{N-2;1}^2 + \sum_{i=2}^{N-2} v_i^2; \end{aligned} \quad (27)$$

where v_{N-1}^2 also appears quadratically. We can continue this construction by defining

$$v_{N-i} := v_{N-i} + \frac{1}{i+2}v_{N-i+1;1}; \quad i=1;\dots;N-2; \quad (28)$$

which turns the exponent Y into a purely Gaussian form:

$$Y = 2v_1^2 + \frac{3}{2}v_{N-1}^2 + \frac{4}{3}v_{N-2}^2 + \dots + \frac{i+2}{i+1}v_{N-i}^2 + \frac{N}{N-1}v_2^2; \quad (29)$$

The last step of this construction consists in noting that we can substitute the integration variables according to

$$\prod_{i=1}^{N-1} dy_i = J \prod_{i=2}^{N-1} dv_i dv_1 = J \prod_{i=1}^{N-1} dv_i = Dv \quad (30)$$

with nonzero but constant Jacobians J, J , the value of which is unimportant for the calculation of expectation values. This allows us to write the path integral Eq. (22) as

$$\int \mathcal{D}y \mathcal{P} f_{y_k} \int \mathcal{D}v \exp \left[-\frac{N}{4} (2v_1^2 + \sum_{i=1}^{N-1} \frac{i+2}{i+1} v_{N-i}^2) \right] J \mathcal{D}v \mathcal{P} f_{v_k} \dots; \quad (31)$$

where $\mathcal{P} f_{v_k}$ can now be generated straightforwardly with the Box-Muller method.

For the construction of unit loops ("v loops"), the above steps have to be performed backwards. The recipe is the following:

- (1) generate $N-1$ numbers $w_i, i=1;\dots;N-1$ via the Box-Muller method such that they are distributed according to $\exp(-w_i^2)$;
- (2) compute the $v_i, i=1;\dots;N-1$, by normalizing the w_i :

$$\begin{aligned} v_1 &= \frac{r}{N} w_1; \\ v_i &= \frac{2}{N} \frac{r}{N+2} \frac{i}{i+1} w_i; \quad i=2;\dots;N-1; \end{aligned} \quad (32)$$

- (3) compute the $v_i, i=2;\dots;N-1$, using

$$v_i = v_1 \frac{1}{N+2} \frac{v_{i-1}}{i}; \quad \text{where } v_{i-1} = \sum_{j=2}^{i-1} v_j; \quad (33)$$

- (4) construct the unit loops according to

$$\begin{aligned} Y_1 &= \frac{1}{N} v_1 \sum_{i=2}^{N-1} \frac{1}{i+1} v_i; \\ Y_i &= Y_{i-1} + v_i; \quad i=2;\dots;N-1; \\ Y_N &= \sum_{i=1}^{N-1} Y_i; \end{aligned} \quad (34)$$

- (5) repeat this procedure n_L times for n_L unit loops.

The formulas in step (4) can be checked straightforwardly by inserting the definitions of the v_i 's and v_1 .

This v-loop algorithm allows us to generate unit loops efficiently without thermalization, i.e., no redundant thermalization sweeps have to be performed, and works for an arbitrary number of points per loop N .

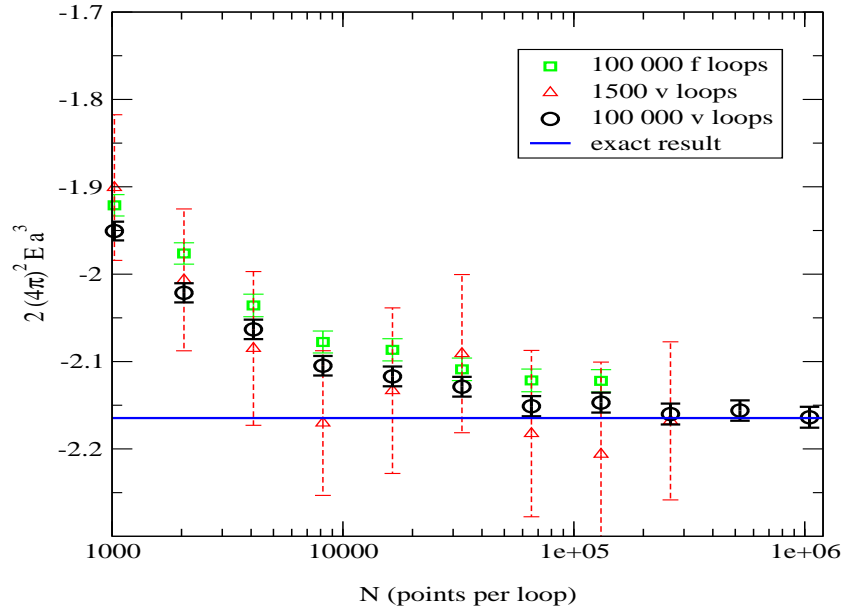


Figure 3: Numerical estimate of the interaction Casimir energy of the parallel-plate configuration for various loop ensembles as a function of the number of points per loop N . The error bars correspond to the Monte-Carlo statistical error; deviations from the exact result on top of the statistical error measure the systematic error due to loop discretization.

3.5 Benchmark test

We test the quality of our loops with the aid of the Casimir energy for the parallel-plate configuration in the Dirichlet limit, the physics of which is described in the next section.

As far as numerics is concerned, there are basically two parameters that control the quality of our loop ensemble: the number of points per loop (ppl) N , and the number of loops n_L . The larger these numbers, the more accurate is our numerical estimate at the expense of CPU time and size. Whereas increasing the number of loops n_L reduces the statistical error of the Monte-Carlo procedure, increasing the number of ppl N reduces the systematic error of loop discretization.

In order to estimate this systematic error, we have to study the approach towards the continuum limit. The idea is to choose N large enough for a given n_L , such that the systematic error is smaller than the statistical one.

In Fig. 3, we plot the numerical estimates for the parallel-plate Casimir energy as a function of the number of ppl N and compare it with the classic result. The error bars represent the statistical error of the Monte-Carlo procedure. The deviation of the numerical estimates from the exact result on top of the error bars serves as a measure of the systematic error. As is visible therein, a rather small number of several thousand ppl, $N \approx 1000$, is sufficient to get a numerical estimate with $\approx 5\%$ error using $n_L = 1500$ loops. For a high-precision estimate with an error $\approx 0.5\%$, larger loop ensembles with $n_L \approx 100000$

are required. For $N \sim 50^000$ ppl, systematic and statistical errors are of the same order, and for $N \sim 100^000$ ppl, the systematic error is no longer relevant for ν loops. For f loops, however, we observe a systematic 1% error in the high-precision data of unclear origin.

Nevertheless, the important conclusion of this test is that worldline numerics has proved its ability to describe quantum fluctuations with Dirichlet boundary conditions quantitatively.

4 Casimir forces between rigid bodies

Casimir forces can be analytically computed for only a small number of rigid-body geometries among which there is Casimir's classic result for the parallel-plate configuration; for perfectly conducting plates at a distance a , the interaction energy per unit area is [1]

$$E_{PP}(a) = -\frac{1}{2} \frac{\pi^2}{720} \frac{1}{a^3} \quad (35)$$

for a fluctuating real scalar field; for a complex scalar as well as for electromagnetic fluctuations, the factor 1/2 has to be dropped. The famous Casimir force is obtained by differentiating Eq. (35) by a .

4.1 Proximity force approximation

The standard approximation method for non-analytically solvable Casimir problems is the proximity force approximation (PFA) [7, 8]. The basic idea is to apply the parallel-plate result to infinitesimal bits of the generally curved surfaces and integrate them up,

$$E = \int_S^Z E_{PP}(z) dS; \quad (36)$$

where E_{PP} is the interaction energy per unit area of the parallel-plate case. S represents the integration domain and denotes either one of the surfaces of the interacting bodies or a suitably chosen mean surface [8]. At this point, the proximity force approximation is ambiguous, and we will simply insert both surfaces in order to determine the variance. In Eq. (36), dS denotes the invariant surface measure, and z represents the separation between the two surfaces associated with the surface element dS on S . Obviously, the proximity force approximation neglects any nonparallelity and any curvature (the latter because each surface element on S_1 is assumed to "see" only one surface element on S_2 at separation z ; but curvature effects require information about a whole neighborhood of the element on S_2).

The proximity force approximation is expected to give reasonable results only if (i) the typical curvature radii of the surfaces elements is large compared to the element distance and (ii) the surface elements with strong nonparallelity are further separated than the more

parallel ones.⁴

For configurations that do not meet the validity criteria of the proximity force approximation, a number of further approximations or improvements exist, such as an additive summation of interatomic pairwise interactions and the inclusion of screening effects of more distant layers by closer ones [3]. Though these methods have proved useful and even quantitatively precise for a number of examples, to our knowledge, a general, unambiguous and systematically improvable recipe without ad hoc assumptions is still missing.

In Sect. 5, we compare our results with the proximity force approximation in the simplest version as mentioned above, in order to gain insight into the effects of curvature.

4.2 Casimir forces on the worldline

As described in Sect. 2, we represent the rigid bodies by a potential $V(\mathbf{x})$. The functional form of the potential leaves room enough for modeling many physical properties of real Casimir configurations. Let us confine ourselves to an idealized potential well which is represented by a function in space (for "soft" boundary conditions, see, e.g., [21]),

$$V(\mathbf{x}) = \int_{\Sigma} d^d(\mathbf{x} - \mathbf{x}'); \quad (37)$$

where the geometry of the Casimir configuration is represented by Σ , denoting a $d-1$ dimensional surface. Σ is generally disconnected (e.g., two disconnected plates, $\Sigma = \Sigma_1 + \Sigma_2$) and can be degenerate, i.e., effectively lower dimensional (a point). The surface measure d^d is assumed to be reparametrization invariant, and \mathbf{x} denotes a space vector pointing onto the surface. The coupling β has mass dimension 1 and is assumed to be positive. It can roughly be viewed as a plasma frequency of the boundary matter: for fluctuations with frequency $\omega \gg \beta$, the Casimir boundaries become transparent. In the limit $\beta \rightarrow 1$, the potential imposes the Dirichlet boundary condition, implying that all modes of the field have to vanish on Σ .

Inserting this potential into the worldline formula (3), we encounter the integral

$$\begin{aligned} I_V[\mathbf{y}(t); T; \mathbf{x}] &= \int_0^1 dt V(\mathbf{x} + \frac{\mathbf{p}}{T} \mathbf{y}(t)) = \int_0^1 dt \int_{\Sigma} d^d(\mathbf{x} + \frac{\mathbf{p}}{T} \mathbf{y}(t) - \mathbf{x}') \\ &= \frac{\mathbf{p}}{T} \int_{ft_g} d^d \frac{1}{|\dot{\mathbf{y}}(t_i)|}; \end{aligned} \quad (38)$$

where ft_g is the set of all points where a given scaled unit loop $\frac{\mathbf{p}}{T} \mathbf{y}(t)$ centered upon \mathbf{x} pierces the Casimir surface Σ at \mathbf{x}' . If a loop does not pierce the surface (for given T and \mathbf{x}), $I_V[\mathbf{y}(t)] = 0$ for this loop. Of course, there are also loops that merely touch the Casimir surface but do not pierce it. For these loops, the inverse velocity $1 = |\dot{\mathbf{y}}(t_i)|$ diverges on the

⁴The second condition is not so well discussed in the literature; it is the reason why the proximity force approximation gives reasonable results for a convex spherical lens over a plate (convex as seen from the plate), but fails for a concave lens.

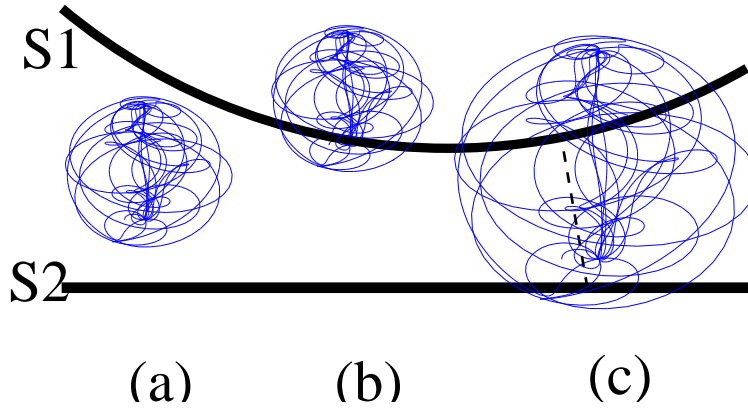


Figure 4: Worldline loop contributions to Casimir energies between two surfaces (S1 and S2): loop (a) does not contribute at all, it is an ordinary vacuum fluctuation. Loop (b) contributes to the local energy density near the upper plate, but does not contribute to the Casimir force. Only loop (c) contributes to the Casimir force, since it "sees" both surfaces. Here, the loop picks up nonlocal information about a whole neighborhood, whereas the proximity force approximation employs only information about local distances indicated by the dashed line.

surface. But since this divergence occurs in the argument of an exponential function, these loops remove themselves from the ensemble average.

As an example, let \mathcal{V} consist of two disconnected surfaces (bodies), such that $V(\mathbf{x}) = V_1(\mathbf{x}) + V_2(\mathbf{x})$. For a given proper time T , the Casimir energy density at point \mathbf{x} receives contributions only from those loops which pierce one of the surfaces. The interaction energy density defined in Eq. (8) is even more restrictive: if a certain loop $y_0(t)$ does not pierce one of the surfaces, then $(W_{V_1+V_2}[y_0] - 1) = (W_{V_1}[y_0] - 1) = (W_{V_2}[y_0] - 1) = 0$. Therefore, only those loops which pierce both surfaces contribute to the interaction energy density, as illustrated in Fig. 4. This reflects the inherent nonlocality of the Casimir force in worldline language.

If the loop $y_0(t)$ does pierce both plates, its contribution to the energy density is

$$\text{contrib. of } y_0(t) = 1 - (e^{-T \int V_1} + e^{-T \int V_2} - e^{-T \int V_1 + V_2})^2 \in [0; 1] \quad (39)$$

From this general consideration, together with the global minus sign in Eq. (3), we learn that Casimir forces between rigid bodies in our scalar model are always attractive. This statement holds, independent of the shape of the bodies and the details of the potential (as long as $V(\mathbf{x})$ is non-negative).

In the Dirichlet limit, $\beta \rightarrow 1$, the exponential functions in Eq. (39) vanish, and the contribution of a loop is $= 1$ if it pierces both surfaces and $= 0$ otherwise.

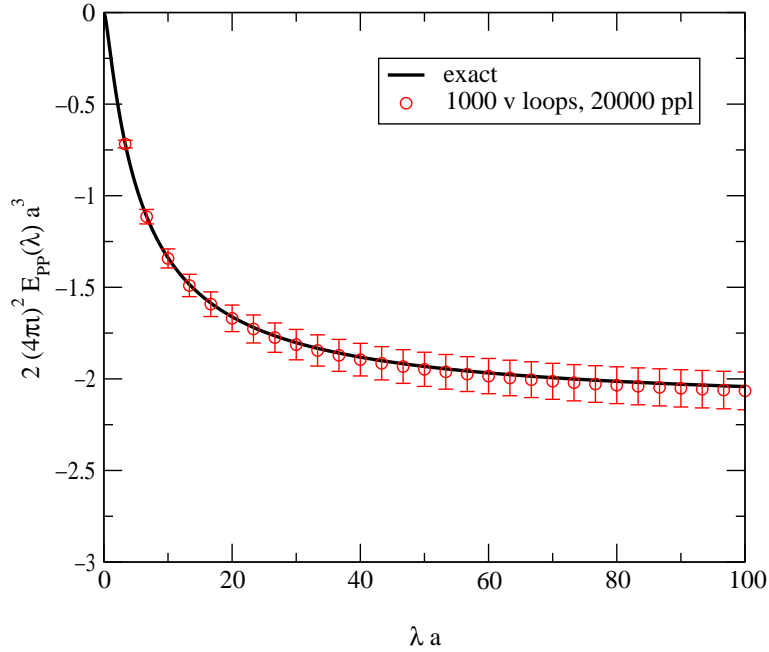


Figure 5: Parallel plates: interaction Casimir energy per unit area for the parallel-plate configuration as a function of the coupling λ (units are set by the plate separation a). The numerical estimate reproduces the exact result for a wide range of couplings including the Dirichlet limit (cf. Fig.3).

5 Numerical results

5.1 Parallel Plates

Let us first consider the classic example of a Casimir configuration consisting of parallel plates separated by a distance a and located at $z = -a/2$ and $z = a/2$ orthogonal to the $z = x_3$ axis. For this, Eq. (37) reduces to

$$V(x) = V(z) = \left[(z + a/2) + (z - a/2) \right]^{-1} \mathbb{W} V_2; \quad (40)$$

In order to test the numerical worldline approach, we compare our numerical estimates with the analytically known result [22] of the interaction Casimir energy for arbitrary coupling λ and scalar mass m in units of the plate separation a . In Fig. 5, we study a wide range of couplings and the approach to the Dirichlet limit, $\lambda a \rightarrow 1$; here, the energy per unit area tends to

$$E_{PP}(\lambda a \rightarrow 1) = \frac{1}{2(4\pi)^2} \frac{1}{45} \frac{1}{a^3}, \quad \frac{1}{2(4\pi)^2} \frac{1}{45} \frac{1}{a^3}; \quad (41)$$

which is the classic Casimir result for a massless scalar field.⁵ As is visible in Fig. 5, the agreement is satisfactory even for small ensembles with $N = 20000$ ppl.

⁵Here and in the following, we have separated the common proportionality prefactors $1/[2(4\pi)^2 a^2]$ for convenience (see, Eq. (3)).

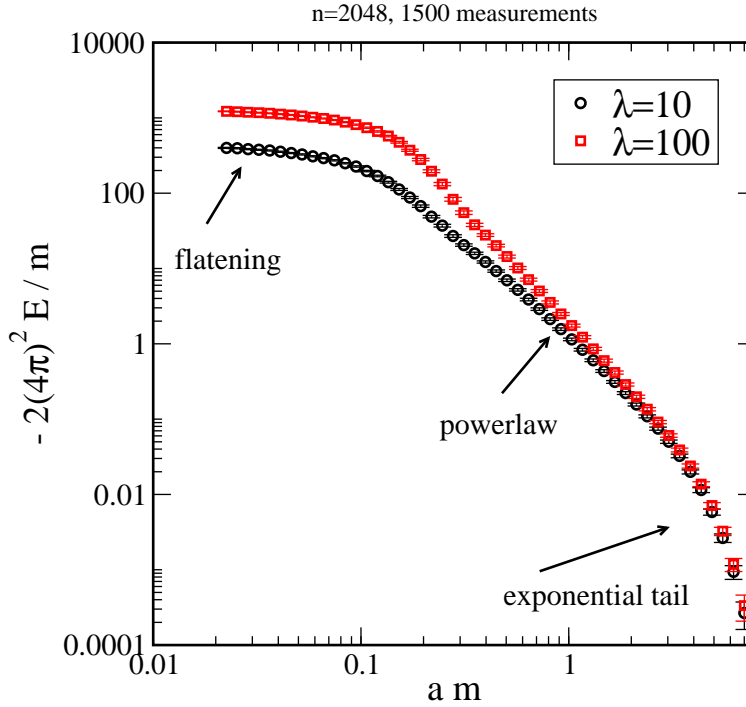


Figure 6: Parallel plates: interaction Casimir energy per unit area for the parallel-plate configuration as a function of the distance a in units of the mass m for $\lambda = 10m$ and $\lambda = 100m$.

Let us finally discuss the Casimir energy as function of the distance a of two parallel plates for finite mass m and finite λ , in order to explore the strength of the worldline approach in various parameter ranges. The result is shown in Fig. 6. A finite value for λ simulates a finite plasma frequency. Hence, for $\lambda \rightarrow \infty$ the plates are essentially transparent for those modes of the quantum field which fit between the plates. The interaction Casimir energy becomes a constant, implying that the pure Casimir force vanishes when the plates touch each other ($a = 0$). For $\lambda \rightarrow 0$, we observe that the Casimir energy decreases exponentially with a , as expected, since possible fluctuations are suppressed by the mass gap. In the intermediate distance regime, $1/\lambda < a < 1/m$, we observe a power law $E_{PP} \sim a^{-3}$, which is familiar from the ideal case $\lambda \rightarrow \infty, m = 0$.

5.2 Sphere above plate

The Casimir force between a sphere or a spherical lens above a plate is of utmost importance, because a number of high-precision measurements have been performed with this experimental configuration. Let us confine ourselves to the massless case, $m = 0$, in the Dirichlet limit $\lambda \rightarrow \infty$; generalizations to other parameter ranges are straightforward, as in the parallel-plate case.

In order to gain some intuition for curvature effects, let us consider a sphere of radius R the center of which resides over a plate at distance $a = 2R$ as an example. The interaction

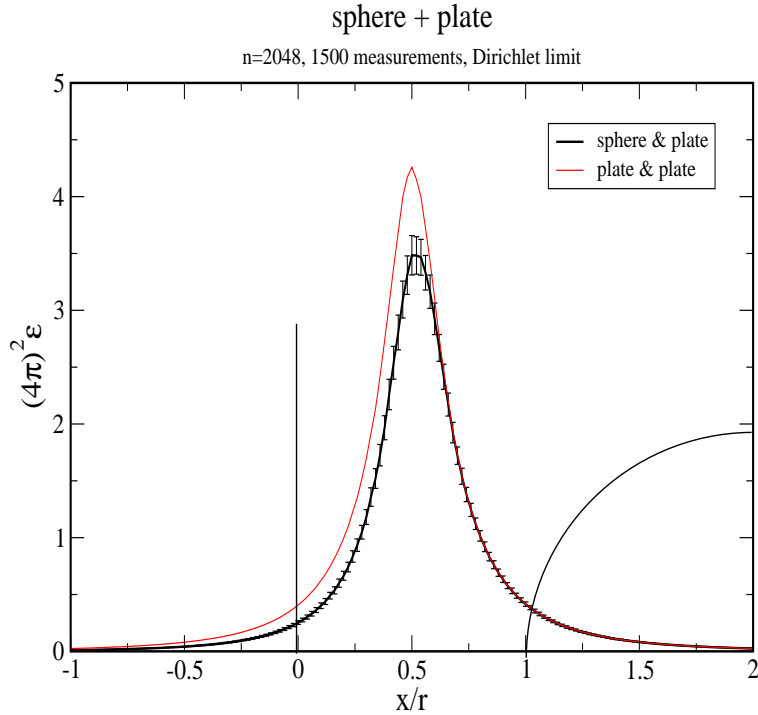


Figure 7: Sphere above Plate: interaction Casimir energy density along the symmetry axis (x axis) for the sphere-plate configuration in comparison to the parallel-plate case. Close to the sphere, the worldline loops do not "see" the curvature; but at larger distances, curvature effects enter the energy density.

Casimir energy density along the symmetry axis is shown in Fig. 7. For comparison, the energy density of the case where the sphere is replaced by a plate is also shown. One observes that the energy density close to the sphere is well approximated by the energy density provided by the parallel-plates scenario. This is already at the heart of the nonlocal nature of the Casimir force and can easily be understood in the worldline approach.

Recall that the dominant contribution to the interaction Casimir energy density arises from loops which intersect both surfaces. If the center of the loop is located close to the sphere, the loops which intersect both surfaces hardly experience the curvature of the sphere; this is because loops that are large enough to pierce the distant plate will also pierce the close-by sphere rather independent of its radius. By contrast, if the loop center is located close to the plate, the dominant (large) loops possess intersections with the sphere at many different points (not necessarily the closest point). In this case, the worldline loops "see" the curvature of the sphere that now enters the energy density.

Let us now consider the complete interaction Casimir energy for the sphere-plate configuration as a function of the sphere-plate distance a (we express all dimensional quantities as a function of the sphere radius R). In Fig. 8, we plot our numerical results in the range $a/R \in [0; 10]$. Since the energy varies over a wide range of scales, already small

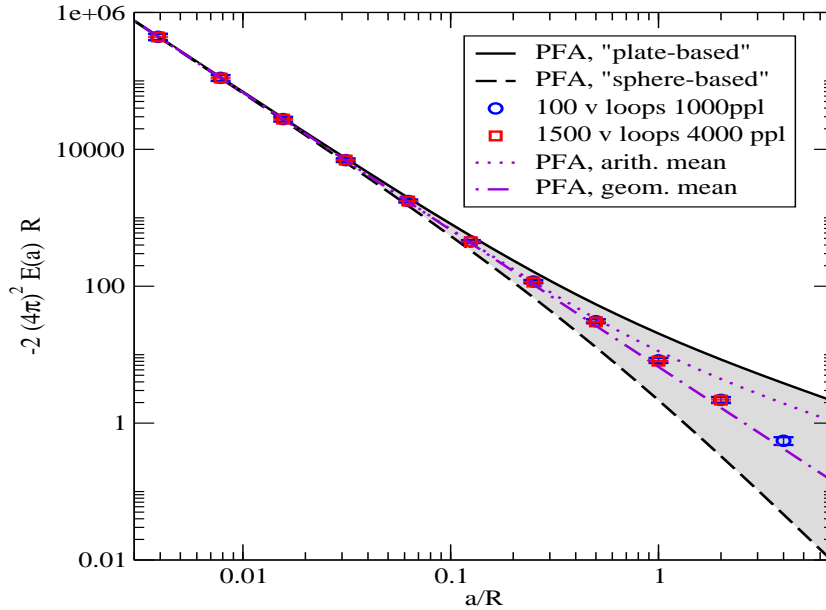


Figure 8: Sphere above Plate: logarithmic plot of the interaction Casimir energy for the sphere-plate configuration. For small separations/large spheres, $a/R \lesssim 0.02$, the proximity force approximation (PFA) approximates the numerical estimate well; but for larger a/R , curvature effects are not properly taken into account. The PFA becomes ambiguous for larger a/R , owing to possible different choices of the integration domain S in Eq. (36). A geometric mean (dotted-dashed line) of $S = S_{\text{plate}}$ and $S = S_{\text{sphere}}$ shows reasonable agreement with the numerical result.

loop ensembles with rather large errors suffice for a satisfactory estimate (the error bars of an ensemble of 1500 v loops with 4000 ppl cannot be resolved in Fig. 8).

Let us compare our numerical estimate with the proximity force approximation (PFA): using the plate surface as the integration domain in Eq. (36), $S = S_{\text{plate}}$, we obtain the solid line in Fig. 8 (PFA, plate-based), corresponding to a "no-curvature" approximation. As expected, the PFA approximation agrees with our numerical result for small distances (large sphere radius). Sizeable deviations from the PFA approximation of the order of a few percent occur for $a/R \gtrsim 0.02$ and larger. Here, the curvature-neglecting approximations are clearly no longer valid. This can be read off from Fig. 9, where the resulting interaction energies are normalized to the numerical result.

In the PFA, we have the freedom to choose alternatively the sphere surface as the integration domain, $S = S_{\text{sphere}}$. Although still no curvature-related fluctuation effects enter this approximation, one may argue that information about the curvature is accounted for by the fact that the integration domain now is a curved manifold. Indeed, Fig. 8 shows that this "sphere-based" PFA approximation deviates from the plate-based PFA in the same direction as the numerical estimate, but overshoots the latter by far. It is interesting to observe that the geometric mean, contrary to the arithmetic mean, of the two different

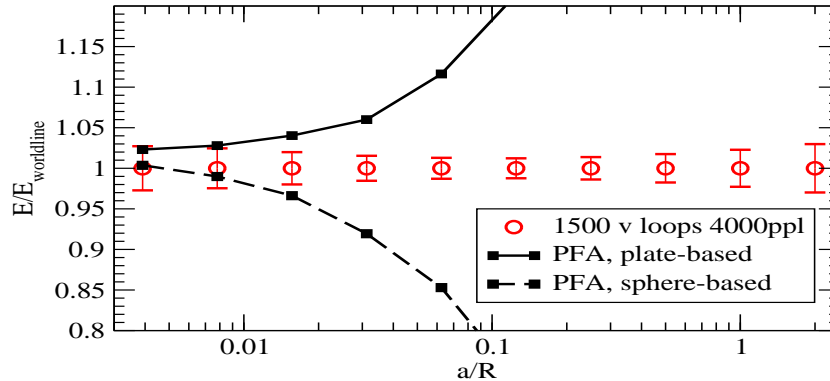


Figure 9: Sphere above Plate: interaction Casimir energies normalized to the numerical result (further conventions as in Fig. 8). For $a=R \approx 0.02$, the fluctuation-induced curvature effects occur at the percent level.

PFA approximations lies rather close to the numerical estimate; we will comment on this in more detail in the next section.

5.3 Cylinder above plate

In order to study the relation between PFA approximations and the full numerical estimate a bit further, let us consider a second example of a cylinder above a plate. Apart from the difference in the third dimension, all parameters and conventions are as before.

Again, we observe in Fig. 10 that the numerical estimate is well approximated by the PFA for $a=R \approx 0.02$, but curvature effects become important for larger distance-to-curvature-radius ratios. As in the sphere-plate case, the plate-based PFA neglects, but the cylinder-based PFA over-estimates, the curvature effects for $a=R$ of order one.

Our results seem to suggest that the various possible choices for the integration domain in the proximity force approximation may give upper and lower bounds for the correct answer. Indeed, the geometric mean between the two possible choices for the sphere-plate configuration is rather close to the numerical estimate (dotted-dashed line in Figs. 8 and 10). Similar positive results for the geometric mean have been found for the two-concentric-cylinder configuration [23] using semiclassical approximations [24] and for a "chaotic" geometry [8].

However, we believe that this "agreement" beyond the strict validity limit of the PFA is accidental. First, detailed inspection reveals that the geometric mean and the numerical estimate are not fully compatible within error bars; this is particularly visible in the cylinder-plate case in Fig. 10. Secondly, there are no fundamental arguments favoring the geometric mean; by contrast, the arithmetic mean (as well as the quadratic mean) are not good approximations. Thirdly, for even larger separations, $a/R \gg 1$, it is known that the interaction Casimir energy in the sphere-plate case behaves as $E \propto R^3 = a^4$ [25], whereas even the sphere-based PFA decreases only with $E \propto R^2 = a^3$. From the viewpoint of the worldline,

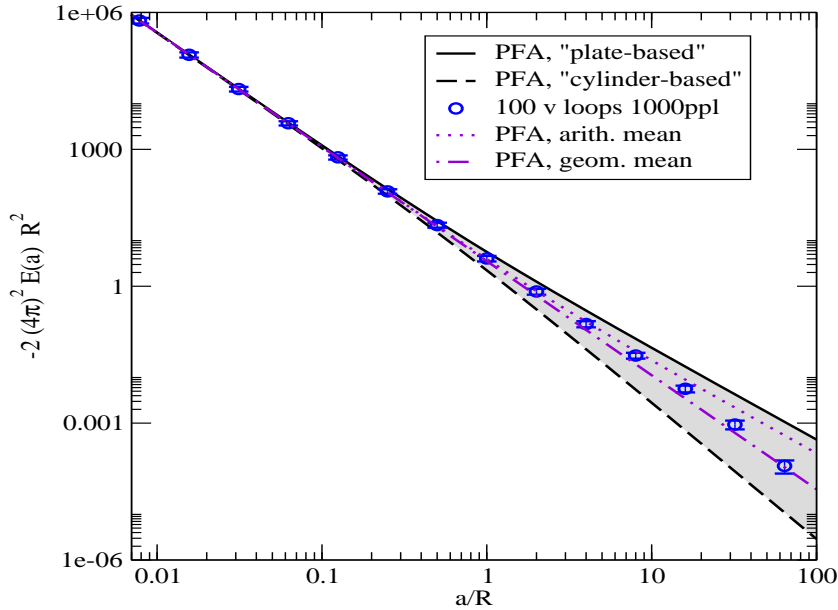


Figure 10: Cylinder above Plate: logarithmic plot of the interaction Casimir energy for the sphere-plate configuration (cf. Fig. 8).

It is obvious anyway that true fluctuation-induced curvature effects cannot be taken into account by PFA-like arguments. Nevertheless, the geometric-mean prescription may yield a reasonable first guess for Casimir forces in a parameter range beyond the formal validity bounds of the PFA where the expansion parameter is maximally of order one.

6 Conclusions

We have proposed and developed a new method to compute Casimir energies for arbitrary geometries from first principles in a systematic manner. The approach is based on perturbative quantum field theory in the string-inspired worldline formulation which maps field theoretic problems onto one-dimensional quantum mechanical path integrals with an evolution in a "5th coordinate", the proper time. These path integrals can easily be performed with numerical Monte-Carlo techniques.

Beyond any technical and numerical advantages, we first would like to stress that the worldline formulation offers an intuitive approach to the phenomena induced by quantum fluctuations. The geometric dependence of Casimir forces between rigid bodies, curvature effects and nonlocalities can already be guessed when thinking in terms of worldline loop clouds.

As to technical advantages, the (usually complicated) analysis of the fluctuation spectrum and the mode summation are performed at one fell swoop in the worldline approach. Above all, our algorithm is completely independent of the details of the Casimir geometry

and no underlying symmetry is required. The algorithm is scalable: if higher precision is required, only the parameters of the loop ensemble (points per loop and number of loops) have to be adjusted⁶.

In this work, we have focused on Casimir forces between rigid bodies for which a computation of the interaction energy suffices; the latter is free of subtle problems with renormalization. Nevertheless, the worldline approach is in principle capable of isolating and classifying divergencies of general Casimir energy calculations, and the unambiguous program of quantum field theoretic renormalization can be performed.

Confining ourselves to a fluctuating real scalar field, we tested our method using the parallel-plate configuration. New results have been obtained for the experimentally important sphere-plate configuration: here we studied the (usually neglected) nonlocal curvature effects which become sizable for a distance-to-curvature-radius ratio of $a=R \ll 0.02$. Even though the proximity force approximation (PFA) as standard approximation method cannot correctly account for fluctuation-induced curvature effects, we found (accidental) agreement between our numerical estimate and the PFA with a "geometric-mean prescription": the latter implies a geometric mean over the possible choices of surface integration in Eq. (36). This geometric mean PFA might provide for a first guess of the Casimir force for $a=R$ of order one, but has to be treated with strong reservations.

In this work, we have accepted a number of simplifications, in order to illustrate our method. Many generalizations to more realistic systems are straightforward, as discussed in the remainder of this section:

- 1) We modeled the Casimir bodies by δ -potentials, mostly taking the Dirichlet limit. In fact, this was not a real simplification, but numerically even more demanding. Modeling the bodies by finite and smooth potential wells requires worldline ensembles with a much smaller number of points per loop. The δ -potentials represent the "worst case" for our algorithm, which has nevertheless proved to be applicable.
- 2) In experimental realizations, effects of finite temperature and surface roughness have to be taken into account. Both can be implemented in our formalism from first principles. Including finite temperature with the Matsubara formalism leads to a worldline integral with periodic boundary conditions of the worldline loops in Euclidean time direction [26, 15] which can easily be performed for Casimir configurations. The surface roughness can be accounted for by adding a characteristic random "noise" to the local support of the potential. In both cases, the observables can directly be computed by our formalism without any kind of perturbative expansion.
- 3) For obtaining the Casimir force, our results for the interaction energy have to be differentiated with respect to the separation parameter. Since numerical differentiation generally leads to accuracy reduction, it is alternatively possible to perform the differentiation first analytically; this yields a slightly more complicated worldline integrand which can nevertheless be easily evaluated without loss of precision. By a similar reasoning, we can also

⁶The numerical computations for this work have been performed on ordinary desktop PC's. Improvement in precision can be obtained at comparatively low cost, since the computer resources required increase only linearly with our loop parameters.

obtain the (expectation value of the) energy-momentum tensor, which is frequently at the center of interest in Casimir calculations. For this, we can exploit the fact that the energy-momentum tensor can be obtained from the effective action by differentiating Eq. (3) with respect to the metric analytically; the resulting worldline integrand can then be put into the standard path integral machinery.

4) Radiative corrections to the Casimir effect can also be included in our method, employing the higher-loop techniques of the worldline approach [13]. We expect these computations to be numerically more demanding, since more integrations are necessary, but the general approach remains the same.

5) The implementation of finite conductivity corrections is less straightforward, since this generally requires a formulation for real electromagnetic fluctuations (an extension to complex scalars is not sufficient). For this, the starting point can be a field theoretic Lagrangian defining a model for the interaction of the electromagnetic field with the bodies as suggested, e.g., in [27]. Although these Lagrangians are generally not renormalizable, one may expect that the dispersive properties of the bodies provide for a physical ultraviolet cutoff (although this has to be studied with great care [28]).

Acknowledgment

We are grateful to W. Dittrich, M. Quandt and H. Weigel for useful information. We would like to thank M. Luscher for providing us with the latest double-precision version of the RANLUX random-number generator. H.G. acknowledges financial support by the Deutsche Forschungsgemeinschaft under contract Gi 328/1-2. L.M. is supported by the Deutsche Forschungsgemeinschaft under contract GRK 683.

References

- [1] H.B. Casimir, Kon. Ned. Akad. Wetensch. Proc. 51, 793 (1948).
- [2] S.K. Lamoreaux, Phys. Rev. Lett. 78, 5 (1997);
 U. Mohideen and A. Roy, Phys. Rev. Lett. 81, 4549 (1998) [arXiv:physics/9805038];
 A. Roy, C. Y. Lin and U. Mohideen, Phys. Rev. D 60, 111101 (1999) [arXiv:quant-ph/9906062];
 T. Ederth, Phys. Rev. A 62, 062104 (2000);
 G. Bressi, G. Carugno, R. Onofrio and G. Ruoso, Phys. Rev. Lett. 88, 041804 (2002) [arXiv:quant-ph/0203002].
- [3] V.M. Mostepanenko and N.N. Trunov, "The Casimir Effect and its Applications," Clarendon Press, Oxford (1997);
 M. Bordag, U. Mohideen and V.M. Mostepanenko, Phys. Rept. 353, 1 (2001) [arXiv:quant-ph/0106045];
 K.A. Milton, "The Casimir Effect: Physical Manifestations of Zero-Point Energy," World Scientific, River Edge (2001).

- [4] H.B.Chan, V.A.Aksyuk, R.N.Kleinman, D.J.Bishop, F.Capasso, *Science* 291, 1941 (2001); *Phys.Rev.Lett.* 87, 211801 (2001).
- [5] D.E.Krause and E.Fischbach, *Lect.Notes Phys.* 562, 292 (2001) [[arXiv:hep-ph/9912276](#)]; V.M.Mostepanenko and M.Novello, *Phys.Rev.D* 63, 115003 (2001) [[arXiv:hep-ph/0101306](#)]. K.A.Milton, R.Kantowski, C.Kao and Y.Wang, *Mod.Phys.Lett.A* 16, 2281 (2001) [[arXiv:hep-ph/0105250](#)].
- [6] D.E.Krause and E.Fischbach, *Phys.Rev.Lett.* 89, 190406 (2002) [[arXiv:quant-ph/0210045](#)].
- [7] B.V.Derjaguin, I.I.Abrikosova, E.M.Lifshitz, *Q.Rev.* 10, 295 (1956).
- [8] J.Blocki, J.Randrup, W.J.Swiatiecki, C.F.Tsang, *Ann.Phys.(N.Y.)* 105, 427 (1977).
- [9] D.Deutsch and P.Candelas, *Phys.Rev.D* 20, 3063 (1979).
- [10] N.Graham, R.L.Jae, V.Khemani, M.Quandt, M.Scandurra and H.Weigel, *Nucl.Phys.B* 645, 49 (2002) [[arXiv:hep-th/0207120](#)]; [[arXiv:hep-th/0207205](#)].
- [11] K.A.Milton, [[arXiv:hep-th/0210081](#)].
- [12] R.P.Feynman, *Phys.Rev.* 80, 440 (1950); 84, 108 (1951); A.M.Polyakov, *"Gauge Fields And Strings,"* Harwood, Chur (1987); Z.Bern and D.A.Kosower, *Nucl.Phys.B* 362, 389 (1991); B 379, 451 (1992); M.J.Strassler, *Nucl.Phys.B* 385, 145 (1992); M.G.Schmidt and C.Schubert, *Phys.Lett.B* 318, 438 (1993) [[hep-th/9309055](#)].
- [13] C.Schubert, *Phys.Rept.* 355, 73 (2001) [[arXiv:hep-th/0101036](#)].
- [14] H.Gies and K.Langfeld, *Nucl.Phys.B* 613, 353 (2001) [[arXiv:hep-ph/0102185](#)].
- [15] H.Gies and K.Langfeld, *Int.J.Mod.Phys.A* 17, 966 (2002) [[arXiv:hep-ph/0112198](#)].
- [16] K.Langfeld, L.Moyaerts and H.Gies, *Nucl.Phys.B* 646, 158 (2002) [[arXiv:hep-th/0205304](#)].
- [17] M.Reuter and W.Dittrich, *Eur.J.Phys.* 6, 33 (1985).
- [18] C.Itzykson and J.M.Drouot, *"Statistical Field Theory,"* Cambridge Univ.Pr. (1989)
- [19] S.Samuel, *Nucl.Phys.B* 154, 62 (1979).
- [20] M.G.Schmidt and I.O.Stamatescu, [[arXiv:hep-lat/0201002](#)]; [[arXiv:hep-lat/0209120](#)].
- [21] A.A.Actor and I.Bender, *Phys.Rev.D* 52, 3581 (1995).
- [22] M.Bordag, D.Hennig and D.Robaschik, *J.Phys.A* 25, 4483 (1992).
- [23] F.D.Mazzitelli, M.J.Sanchez, N.N.Scoccola and J.von Stecher, [[arXiv:quant-ph/0209097](#)].
- [24] M.Schaden and L.Spruch, *Phys.Rev.A* 58, 935 (1998); *Phys.Rev.Lett.* 84, 459 (2000).
- [25] T.Datta and L.H.Ford, *Phys.Lett.A* 83, 314 (1981).
- [26] D.G.McKeon and A.Rebhan, *Phys.Rev.D* 47, 5487 (1993) [[arXiv:hep-th/9211076](#)].
- [27] G.Feinberg, J.Sucher, *Phys.Rev.A* 2, 2395-2415 (1970).
- [28] G.Barton, *Int.J.Mod.Phys.A* 17, 767 (2002); V.Sopova and L.H.Ford, *Phys.Rev.D* 66, 045026 (2002) [[arXiv:quant-ph/0204125](#)].